HHS Public Access

Author manuscript

Med Phys. Author manuscript; available in PMC 2024 October 29.

Published in final edited form as:

Med Phys. 2024 June ; 51(6): 4044–4055. doi:10.1002/mp.17095.

Depth-encoding using optical photon TOF in a Prism-PET detector with tapered crystals

Xinjie Zeng[1,2], **Andy LaBella**[3], **Zipai Wang**[1,4], **Yixin Li**[1,2], **Wanbin Tan**[1,4], **Amir H. Goldan**[1]

[1]Department of Radiology, Weill Cornell Medical College, Cornell University, New York, NY, US

[2]Department of Electrical and Computer Engineering, College of Engineering and Applied Sciences, Stony Brook University, Stony Brook, NY, US

[3]Department of Radiology, Renaissance School of Medicine, Stony Brook University, Stony Brook, NY, US

[4]Department of Biomedical Engineering, College of Engineering and Applied Sciences, Stony Brook University, Stony Brook, NY, US

Abstract

Background: High-resolution brain positron emission tomography (PET) scanner is emerging as a significant and transformative non-invasive neuroimaging tool to advance neuroscience research as well as improve diagnosis and treatment in neurology and psychiatry. Time-of-flight (TOF) and depth-of-interaction (DOI) information provide markedly higher PET imaging performance by increasing image signal-to-noise ratio and mitigating spatial resolution degradation due to parallax error, respectively. PET detector modules that utilize light sharing can inherently carry DOI information from the multiple timestamps that are generated per gamma event. The difference between two timestamps that are triggered by scintillation photons traveling in opposite directions signifies the event's depth-dependent optical photon TOF (oTOF). However, light leak at the crystal-readout interface substantially degrades the resolution of this oTOF-based depth encoding.

Purpose: We demonstrate the feasibility of oTOF-based depth encoding by mitigating light leak in single-ended-readout Prism-PET detector modules using tapered crystals. Minimizing light leak also improved both energy-based DOI and coincidence timing resolutions.

Methods: The tapered Prism-PET module consists of a 16 × 16 array of 1.5 × 1.5 × 20 mm^3 lutetium yttrium oxyorthosillicate (LYSO) crystals, which are tapered down to 1.2 × 1.2 mm^2 at the crystal-readout interface. The LYSO array couples 4-to-1 to an 8 × 8 array of 3 × 3 mm^2 silicon photomultiplier (SiPM) pixels on the tapered end and to a segmented prismatoid light guide array on the opposite end. Performance of tapered and non-tapered Prism-PET detectors was experimentally characterized and evaluated by measuring flood histogram, energy resolution, energy- and oTOF-based DOI resolutions, and coincidence timing resolution. Sensitivities of

For correspondence or reprints contact: Amirhossein Goldan, Room LH-447, Lasdon Hall, 420 E 70th St, New York, NY, 10021, amg4017@med.cornell.edu, Fax: (631) 444-7538.
First author contact: Xinjie Zeng, Room LH-443, Lasdon Hall, 420 E 70th St, New York, NY, 10021, xiz4015@med.cornell.edu, Fax: (631) 444-7538

scanners using different Prism-PET detector designs were simulated using Geant4 application for tomographic emission (GATE).

Results: For the tapered (non-tapered) Prism-PET module, the measured full width at half maximum (FWHM) energy, timing, energy-based DOI, and oTOF-based DOI resolutions were 8.88 (11.18) %, 243 (286) ps, 2.35 (3.18) mm, and 5.42 (13.87) mm, respectively. The scanner sensitivities using non-tapered and tapered crystals, and 10 rings of detector modules, were simulated to be 30.9 and 29.5 kcps/MBq, respectively.

Conclusions: The tapered Prism-PET module with minimized light leak enabled the first experimental report of oTOF-based depth encoding at the detector module level. It also enabled the utilization of thinner (i.e., 0.1 mm) inter-crystal spacing with barium sulfate as the reflector while also improving energy-based DOI and timing resolutions.

Keywords

Prism-PET; tapered crystal; depth-of-interaction; time-of-flight; high-resolution; high-sensitivity

1 Introduction

Positron emission tomography (PET) has tremendous potential for early detection of brain disorders before the symptomatic onset and accurate differential diagnosis of psychiatric disorders or neurodegenerative diseases such as Alzheimer's disease (AD) due to its distinctive ability to directly image molecular markers of neuropathology [1, 2]. PET is also playing a burgeoning role in neuro-oncology with emerging radiotracers for noninvasive grading of primary brain tumors, delineation of tumor extent, differentiation of tumor recurrence from treatment-related changes, surgical or radiotherapeutic planning, assessment of response, and post-treatment monitoring [3, 4]. However, low spatial resolution in PET limits the quantitative accuracy of small subcortical nuclei such as locus coeruleus (LC) which has evident neuropathological changes in the early stages of AD [5], and partial volume effect degrades the measurements of tumor uptake [6, 7]. Thus, the improvement in spatial resolution is necessary for reliable quantitative PET neuroimaging.

One of the fundamental limits for spatial resolution is annihilation photon acollinearity, which can be minimized by a small-diameter and conformal brain PET scanner that arranges detectors close to the subject [8]. In addition, the compact and conformal geometry design not only reduces costs by using fewer detectors but also increases sensitivity by providing a larger solid angle coverage when compared to whole-body cylindrical PET scanners. Nevertheless, such a geometry causes substantial image blur due to parallax error (PE) not only at the peripheral but also at the center of the field-of-view (FOV). Thus, depth-of-interaction (DOI) localization is an indispensable capability for the PET detector module to correct PE and attain uniform spatial resolution across the FOV [9, 10]. Various DOI detectors have been developed in recent years, including dual-ended readout detectors that can resolve small crystals but increase the cost by using two photodetectors per detector module [11-13], monolithic scintillator detectors that have higher intrinsic spatial resolution but suffer from time-consuming calibration procedures and complex positioning algorithms [14-18], and single-ended readout detector with light-sharing and segmented crystal array

that achieves high resolution at a low cost [19-22]. We recently proposed a practical single-ended DOI-encoding detector module that utilizes a cuboid crystal array and a segmented prismatoid light-guide array, hence the name Prism-PET, for enhanced and localized light-sharing [23-26]. Our first compact and conformal brain prototype scanner based on the Prism-PET detectors has obtained the highest-resolution PET phantom images and enabled accurate visualization as well as uptake quantification of small brain nuclei [27, 28].

The effective sensitivity gain due to TOF is estimated as:

$$TOF_{\text{gain}} = \sqrt{\alpha^2 \frac{2D}{c\Delta t}} = \sqrt{\alpha^2 \frac{D}{\Delta x}} \quad (1)$$

, where α is a factor related to image reconstruction, D is object size, c is the speed of light, Δt is TOF resolution, and Δx, the uncertainty in spatial localization along the LOR, is determined by the TOF resolution [29-31]. This gain is reduced for brain-dedicated PET systems, compared to whole-body scanners, due to the smaller object size, and thus, better TOF resolution is needed to compensate for the smaller D. Reaching a high TOF gain requires mitigating the DOI-induced bias on timing resolution (in the order of 150-200 ps) since coincidence events at different DOIs can lead to biased estimation of photon arrival times, especially for long crystals (15-25 mm) [21, 32, 33]. Multiple approaches have been explored over the years to incorporate the DOI-induced error into the analytical modeling of timing resolution in PET detectors [21, 33, 34]. Our contribution to mitigating this degrading effect is implementing the time offset correction of three-dimensional (3D) channel ID represented by the two-dimensional (2D) crystal ID (axial number, transaxial number) as well as the DOI bin number for our Prism-PET prototype scanner, which resulted in enhanced timing resolution. [28].

When scintillation photons are generated within a crystal column in a Prism-PET detector module, some photons travel downward to trigger the primary SiPM (i.e., primary pixel) and some travel upward to the light guide which are then steered to the nearest-neighboring crystals and travel downward to trigger the nearest-neighboring SiPMs (i.e., secondary pixels, see Figure 1) [28]. Ideally, single-ended light-sharing PET modules with TOF information (such as Prism-PET) should be able to estimate DOI using the optical photon TOF (oTOF) which is the difference between the primary and secondary timestamps. DOI information is intrinsically encoded in multiple light-sharing timestamps with the smallest oTOF due to almost simultaneous triggering of primary and secondary SiPMs for photon interaction close to the light guide, and the largest oTOF due to photon interaction close to the crystal-SiPM interface (Figure 1). However, oTOF-based depth encoding has not yet been reported experimentally due to *light leak* which causes a SiPM to be triggered by photons from neighboring crystal and not the crystal that it is coupled to. Light leak (dashed arrow in Figure 2a) is caused by 1) the finite gap between crystal and SiPM, which is the summation of the thickness of the coupling glue and protective resin [35, 36], and 2) when the crystal column extends beyond the pixel's active area [28, 35].

In this paper, we develop a next-generation Prism-PET detector module using unilaterally tapered crystals to minimize the scintillation light leak at the crystal-readout interface (Figure 2(b)), improve both timing and DOI resolutions and enable the potential utilization of our novel oTOF-based DOI estimation methods. Here we experimentally characterize the tapered and non-tapered (cuboid) [24, 28] Prism-PET module performance in terms of flood histogram, energy resolution, DOI resolutions (weighted and combined methods), and timing resolution. Furthermore, sensitivities of 10-ring Prism-PET scanners with tapered and cuboid modules were evaluated in Geant4 application for tomographic emission (GATE) simulation [37].

2 Materials and methods

2.1 Tapered Prism-PET detector module

The tapered TOF-DOI Prism-PET detector module developed in this study comprised of a 16 × 16 array of 1.5 × 1.5 × 20 mm^3 lutetium yttrium oxyorthosillicate (LYSO) crystals (Shanghai EBO Optoelectronic Technology CO., China) which were tapered down to 1.2 × 1.2 mm^2 at the crystal-readout interface, as shown in Figure 2. The tapered LYSO array coupled 4-to-1 to an 8 × 8 array of 3 × 3 mm^2 silicon photomultiplier (SiPM) pixels (Hamamatsu Photonics K.K., Japan) on the tapered side and to a prismatoid light guide array on the opposite side. The segmented light guide was made of an array of right triangular prisms with three unique designs at the center, edge, and corner, which efficiently redirected scintillation photons to only the nearest neighboring SiPMs and thus enabled enhanced and localized light sharing [23, 24]. Barium sulfate ($BaSO_4$) was used as the reflector material between the crystals and prisms to ensure optical isolation.

2.2 Data acquisition and calibration

Data acquisition was implemented by using a TOFPET2 application-specific integrated circuits (ASICs) evaluation kit (PETsys Electronics S.A., Portugal) which consisted of a TOF front-end board (FEB/D) and two front-end modules (FEM), with each FEM containing four TOFPET2 ASIC that read 256 channels [38-40]. SiPMs in the tapered module were read out by a TOFPET2 ASIC with 64 channels, and the signal from each channel was fed into an analog-to-digital converter (ADC) as well as a time-to-digital converter (TDC) to acquire energy and timing information, respectively. To evaluate whether the incoming signal is valid, three discriminator thresholds were utilized in the evaluation kit including one energy threshold (vth_e) and two timing thresholds (vth_t1 and vth_t2). [40]. All ASICs in the evaluation kit were calibrated using the calibration routine in the PETsys software before any data acquisition. All acquired list-mode data was processed with an energy window of 460–560 keV, a coincidence time window of 15 ns, and inter-crystal scatter (ICS) rejection. Given that ASIC circuitry's calibration is affected by large temperature variances, all chips were maintained within 20 ± 0.2 °C by conducting experiments in a temperature-controlled chamber.

2.3 Flood histogram

The measurement was performed by uniformly irradiating the tapered Prism-PET module with a 1-mm diameter ^{22}Na point source positioned 10 cm away from the module. The

same measurements were implemented using our two previously designed 4-to-1 coupled Prism-PET modules for comparison: one with 1.4 × 1.4 × 20 mm^3 LYSO crystals (1.4-mm cuboid Prism-PET module) and the other with 1.5 × 1.5 × 20 mm^3 LYSO crystals (1.5-mm cuboid Prism-PET module). The two-dimensional (2D) coordinates of flood histogram were calculated from the acquired list-mode data using a truncated center of gravity (TCoG) method [41]. The flood histogram was segmented using k-means clustering and corrected by moving the center of each segmented cluster to its corresponding equally sampled crystal region [28, 42].

2.4 Energy resolution

Crystal look-up table (LUT) was generated from the corrected flood histogram and used to obtain the energy spectrum for each crystal. The energy spectrum was fitted into a Gaussian function with its full width at half maximum (FWHM) value representing the crystal energy resolution. The detector module energy resolution was the average energy resolution of all crystals.

2.5 DOI resolution

The DOI measurements were performed in coincidence mode using a Prism-PET detector module consisting of a 24 × 24 array of 0.9 × 0.9 × 20 mm^3 LYSO crystals coupled 9-to-1 to an 8 × 8 array of SiPMs as a reference module. The tapered Prism-PET module was selectively irradiated at 19 depths ranging from 1 mm to 19 mm with a step size of 1 mm. A lead collimation was used with the same ^{22}Na point source placed at the center of the lead cylinder with a 1-mm pinhole. The schematic of the experimental setup for the DOI measurements is shown in Figure 3(a). Only coincidence events occurring between the tapered module and the crystal with the highest counting statistics in the reference module were accepted in order to reject Compton scatter. While previous works utilized a single scintillator with SiPM as the reference crystal [35], we used a reference crystal from our 9-to-1 Prism-PET module to simplify the alignment process to the collimator pinhole (see Ref. [25] for the details of experiment setup).

2.5.1 Weighted method—Two weighted methods were used to estimate DOI variables for the 1.5-mm tapered Prism-PET module. (1) energy-weighted DOI variable is derived as:

$$w_{\mathrm{E}} = \frac{E_{\max}}{E} \tag{2}$$

, where $E_{\max}$ is the maximum intensity signal from the primary SiPM, and E is the total detected signals from the primary and light-sharing SiPMs [28, 35]. (2) oTOF-weighted DOI variables is estimated as:

$$w_{\mathrm{oTOF}} = \frac{\sum_{\mathrm{i}=1}^{\mathrm{n}} oTOF_{\mathrm{i}}}{\mathrm{n}} = \frac{\sum_{\mathrm{i}=1}^{\mathrm{n}} (t_{\mathrm{i}} - t_{\mathrm{p}})}{\mathrm{n}} \tag{3}$$

, where t_p is the timestamp generated by the primary SiPM pixel and t_i is the nearest-neighbor light-sharing timestamp (LSTS) generated by the secondary SiPM pixel, and n is 3, 2, and 1 for center, corner, and edge crystals, respectively. The w histograms at five depths (2, 6, 10, 14, and 18 mm) were converted to DOI histograms using linear regression to calculate the slope between w and the ground-truth DOI [24]. DOI distributions were then fitted into Gaussian functions and their FWHM values represented DOI resolutions. Linear regression was also used to calculate the correlation between w_E and w_{oTOF} parameter. The same DOI measurements were performed using 1.4-mm and 1.5-mm cuboid modules for comparison.

2.5.2 Combined method—We combined the energy-weighted DOI and oTOF-weighted DOI methods to estimate the DOI of all events at 5 depths. The resultant DOI (DOI_c) is given as:

$$DOI_c = c_1 \cdot DOI_E + c_2 \cdot DOI_{oTOF} \tag{4}$$

, where the constants c_1 and c_2 represent the weighting coefficients that their sum equals unity, DOI_E is DOI value calculated using the energy information, and DOI_{oTOF} is DOI value estimated using oTOF information. Six different combinations of c_1 and c_2 are employed in the equation, with ratios $r = c_2 / c_1$ selected as 0/1, 0.1/0.9, 0.2/0.8, 0.3/0.7, 0.4/0.6, and 0.5/0.5. The DOI_c histograms of all depths were plotted and fitted into Gaussian functions with their average FWHM values representing DOI resolution for each r.

2.6 Timing resolution

To evaluate timing resolution, a 0.25-mm ^{22}Na point source with radioactivity of 1.85 MBq was positioned at the center of pairs of 1.4-mm cuboid, 1.5-mm cuboid, and 1.5-mm tapered Prism-PET modules. Figure 3(b) shows the schematic of the experimental setup for the timing measurement. The acquired point source data was processed using the time offset correction of 3D channel ID represented by the 2D crystal ID (axial number, transaxial number) and the DOI bin number [28]. The timestamps for each gamma interaction were also corrected with primary and nearest-neighbor LSTSs, thanks to the enhanced and localized light sharing in Prism-PET which generates a characteristic pattern of SiPM signals. Besides, a LOR-based fine-tuning step was employed to optimize timing resolution further [28]. The timing resolution was measured as the FWHM of the Gaussian-fitted timing spectrum.

2.7 Sensitivity of simulated scanners

The sensitivities of a 10-ring conformal Prism-PET brain scanner (a long diameter of 38.5 cm, a short diameter of 29.1 cm, and an axial length of 26.4 cm) using the 1.4-mm and 1.5-mm cuboid detector modules were first evaluated using GATE simulation. A 70-cm line source with 1-mm diameter was filled with 1 MBq ^{18}F and inserted inside a set of 5 concentric 70-cm aluminum sleeves with known diameters to estimate attenuation-free sensitivity [43]. This line source phantom was placed at the center of the FOV and five

simulations (starting with all 5 aluminum sleeves and removing one sleeve each time) were performed for 100s each. The energy window, energy resolution, and coincidence time window were set to 450–650 keV, 10%, and 2.5 ns, respectively. To evaluate the sensitivity of the 10-ring Prism-PET brain scanner with tapered modules, acquired list-mode data from simulations of the scanner with 1.5-mm cuboid modules were also processed to filter the events that occurred outside the tapered crystals. Axial sensitivity profiles and system sensitivities, based on the National Electrical Manufacturers Association (NEMA) NU2-2018 guidelines [43], were obtained using a single-slice rebinning (SSRB) method [27] for original simulation data (scanners with cuboid modules) and truncated simulation data (scanner with tapered modules).

3 Results

3.1 Flood histogram and energy resolution

The flood histograms and energy resolutions of each crystal for the 1.4-mm cuboid, 1.5-mm cuboid, and 1.5-mm tapered Prism-PET modules are shown in Figure 4. Excellent crystal identification was achieved for the entire LYSO array in the tapered module, demonstrating that the decoding error was negligible. The average energy resolutions across all crystals in the 1.4-mm cuboid, 1.5-mm cuboid, and 1.5-mm tapered modules were 10.94 ± 1.21%, 11.18 ± 1.37%, and 8.88 ± 1.03%, respectively (uncorrected for saturation). The tapered Prism-PET module achieved the best energy resolution compared to the cuboid Prism-PET modules.

3.2 DOI resolution

3.2.1 Weighted method—Figure 5 shows DOI_{E} distributions, DOI_{oTOF} distributions, and correlation between w_{E} and w_{oTOF} for center crystals in cuboid and tapered Prism-PET modules at depths of 2, 6, 10, 14, and 18mm. The average DOI_{E} resolutions across five depths were 2.59 ± 0.36 mm, 3.18 ± 0.23 mm, and 2.35 ± 0.19 mm FWHM for the center crystals in 1.4-mm cuboid, 1.5-mm cuboid, and 1.5-mm tapered Prism-PET modules, respectively. The corresponding average DOI_{oTOF} resolutions were 6.45 ± 0.51 mm, 13.87 ± 0.87 mm, and 5.42 ± 0.49 mm FWHM, respectively. The linear correlation coefficients between w_{E} and w_{oTOF} were 0.80 for the 1.4-mm cuboid module, 0.43 for the 1.5-mm cuboid module, and 0.83 for the tapered module. The tapered module achieved the best DOI resolutions and the highest correlation, while the poorest DOI resolutions were obtained for the 1.5-mm cuboid module. Figure 6 shows DOI_{E} and DOI_{oTOF} distributions for center, edge, and corner crystals of the tapered module at five depths. The measured DOI_{E} resolutions were 2.35 ± 0.19 mm, 3.70 ± 0.19 mm, and 4.76 ± 0.23 mm FWHM for center, edge, and corner crystals, respectively. The best DOI_{oTOF} resolution of 5.42 ± 0.49 mm FWHM was obtained using $(oTOF_{1} + oTOF_{2} + oTOF_{3}) / 3$ for the center scenario incorporating three nearest-neighbor SiPM pixels. Optimal DOI resolutions of 8.47 ± 0.74 mm and 11.30 ± 0.39 mm were attained using $oTOF_{1}$ and $(oTOF_{1} + oTOF_{2}) / 2$ for the edge scenario with only one nearest-neighbor SiPMs and the corner scenario with two nearest-neighbor SiPMs, respectively. The tapered module's center, edge, and corner crystals attained their best DOI_{oTOF} resolutions by employing three, one, and two oTOF values, respectively, validating

the effectiveness of three distinct light-sharing designs. By weighting the DOI resolutions based on the percentage of crystals in each region within the crystal array (76.56% center, 21.88% edge, and 1.56% corner), average DOI_E and DOI_{oTOF} resolutions of 2.68 mm and 6.18 mm FWHM were achieved for the tapered Prism-PET module.

3.2.2 Combined method—The combined DOI_c resolutions of six ratios (r = 0 / 1, 0.1/0.9, 0.2/0.8, 0.3/0.7, 0/4/0.6, and 0.5/0.5) for center, edge, and corner crystals are shown in Figure 7. An optimal DOI_c resolution of 2.25 ± 0.14 mm was achieved when employing r = 0.2 / 0.8 for the center crystal. At r = 0.3 / 0.7, the edge and corner crystals demonstrated their best DOI_c resolutions of 3.33 ± 0.39 mm and 4.13 ± 0.50 mm, respectively. Considering all the crystals in the array, the average DOI_c resolution of the tapered module was 2.52 mm.

3.3 Timing resolution

Timing spectra with the ^{22}Na point source placed at the center of pairs of 1.4-mm cuboid modules, 1.5-mm cuboid modules, and 1.5-mm tapered modules are shown in Figure 8. The timing resolutions were 254 ps, 286 ps, and 243 ps FWHM utilizing the time offset and LSTS corrections of 3D channels together with LOR-based fine-tuning for the 1.4-mm cuboid, 1.5-mm cuboid, and tapered modules, respectively.

3.4 Sensitivity of simulated scanners

The axial sensitivity profiles of the 10-ring Prism-PET scanner with 1.4-mm cuboid, 1.5-mm cuboid, and tapered modules are shown in Figure 9. The corresponding system sensitivities extrapolated from five data sets (beginning with 5 aluminum sleeves and finishing with a single sleeve) were 25.0, 30.9, and 29.5 kcps/MBq, respectively.

4 Discussion

Originally, we used a crystal cross-sectional area (CSA) and inter-crystal reflector thickness of 1.4 × 1.4 mm^2 and 0.2 mm, respectively [24]. However, to increase detector efficiency (DE), we changed the design to a crystal CSA and inter-crystal reflector thickness of 1.5 × 1.5 mm^2 and 0.1 mm, respectively [28]. In a 4-to-1 coupled Prism-PET module (i.e., 4 crystals overlaying one 3 × 3 mm^2 SiPM pixel) with cuboid crystals (called cuboid Prism-PET), this new design caused each crystal to exceed the pixel's active area on 2 perpendicular sides by 0.05 mm which exacerbated the scintillation light leak and consequently degraded the overall DOI resolution of the detector module by ~ 20% compared to that of a cuboid Prism-PET module with the original design (see Figure 5). Thus, the tapered crystal design was used (Figure 2) in a Prism-PET module (called tapered Prism-PET) to minimize scintillation light leak at the crystal-SiPM interface and enhance the DOI resolution. Minimizing light leak using tapered crystals and maximizing localized light sharing using segmented prismatoid light guides enabled depth-encoding using scintillation photon TOF (or oTOFs), which are the difference between the primary timestamp (triggered by scintillation photons traveling downward to the primary SiPM) and nearest-neighbor light sharing timestamps (triggered by scintillation photons traveling upward to the light-guide and steered downward to the secondary SiPMs). Given that both

energy values and timestamps are provided in list-mode by the PETsys readout, energy-based DOI (DOI_E) and oTOF-based (DOI_{oTOF}) were weighted averaged to improve the DOI localization accuracy with the optimal weighting factors c2/c1 being 0.2/0.8 (i.e., $r = 0.25$) for center crystals and 0.3/0.7 (i.e., $r = 0.43$) for edge and corner crystals (Figure 7).

In addition, the degradation in DE due to tapered crystals is very small because gamma photon interaction follows the Beer-Lambert law and the small volume reduction due to tapering is at the tail of the exponential distribution. The system sensitivity of the 10-ring Prism-PET scanner (see Ref. [28] for the details of the scanner geometry) with 1.5-mm tapered crystals is 4.5% lower and 15.3% higher than that of the scanners with 1.5-mm and 1.4-mm cuboid crystals, respectively. Apart from reporting the best DOI resolution among other depth encoding detectors with single-ended readout [20, 21], the 1.5-mm tapered Prism-PET module also achieved enhanced energy resolution (Figure 4) and timing resolution (Figure 8) due to substantial reduction in light leak. More specifically, improvement in timing resolution is because more scintillation photons that travel downward towards the primary SiPM are in fact detected by the primary SiPM instead of diverging away and being either undetected due to the non-active inter-pixel gap or detected by the neighboring SiPMs (i.e., crosstalk). Note that timing resolution can be further improved by optimizing the rising edge discriminator threshold and overvoltage of PETsys TOFPET2 ASIC [44].

5 Conclusion

The tapered Prism-PET modules with minimized light leak 1) enabled the utilization of thinner (i.e. 0.1mm) inter-crystal spacings (filled with $BaSO_4$ reflectors) and 1.5 × 1.5 mm^2 crystal CSA for enhanced sensitivity, 2) improved energy-based DOI localization, and 3) to the best of our knowledge, enabled the first experimental report of oTOF-based depth encoding at the detector module level. For future work, we will utilize 1.5 mm tapered Prism-PET detector modules with our recently developed interleaved multiplexing (iMUX) readout [45, 46] to extend the axial FOV of our conformal brain-dedicated PET scanner [28] for high-resolution PET neuroimaging in human subjects.

ACKNOWLEDGMENTS

We gratefully acknowledge help from PETsys Electronics, Portugal. This work was supported by NIH under Grant No. R01EB030413.

References

[1]. Schöll M, Damián A, and Engler H, Fluorodeoxyglucose PET in neurology and psychiatry, PET clinics 9, 371–390 (2014). [PubMed: 26050943]

[2]. Cecchin D, Garibotto V, Law I, and Goffin K, PET imaging in neurodegeneration and neuro-oncology: variants and pitfalls, in Seminars in nuclear medicine, volume 51, pages 408–418, Elsevier, 2021. [PubMed: 33820651]

[3]. Verger A, Kas A, Darcourt J, and Guedj E, PET Imaging in Neuro-Oncology: An Update and Overview of a Rapidly Growing Area, Cancers 14, 1103 (2022). [PubMed: 35267411]

[4]. Galldiks N, Lohmann P, Albert NL, Tonn JC, and Langen K-J, Current status of PET imaging in neuro-oncology, Neuro-Oncology Advances 1, vdz010 (2019). [PubMed: 32642650]

[5]. Braak H, Thal DR, Ghebremedhin E, and Del Tredici K, Stages of the pathologic process in Alzheimer disease: age categories from 1 to 100 years, Journal of Neuropathology & Experimental Neurology 70, 960–969 (2011). [PubMed: 22002422]

[6]. Soret M, Bacharach SL, and Buvat I, Partial-volume effect in PET tumor imaging, Journal of nuclear medicine 48, 932–945 (2007). [PubMed: 17504879]

[7]. Alavi A, Werner TJ, Høilund-Carlsen PF, and Zaidi H, Correction for partial volume effect is a must, not a luxury, to fully exploit the potential of quantitative PET imaging in clinical oncology, Molecular imaging and biology 20, 1–3 (2018).

[8]. Moses WW, Fundamental limits of spatial resolution in PET, Nuclear Instruments and Methods in Physics Research Section A: Accelerators, Spectrometers, Detectors and Associated Equipment 648, S236–S240 (2011).

[9]. Ito M, Hong SJ, and Lee JS, Positron emission tomography (PET) detectors with depth-of-interaction (DOI) capability, Biomedical Engineering Letters 1, 70–81 (2011).

[10]. Mohammadi I, Castro I, Correia P, Silva A, and Veloso J, Minimization of parallax error in positron emission tomography using depth of interaction capable detectors: methods and apparatus, Biomedical Physics & Engineering Express 5, 062001 (2019).

[11]. Yang Y, Wu Y, Qi J, James SS, Du H, Dokhale PA, Shah KS, Farrell R, and Cherry SR, A prototype PET scanner with DOI-encoding detectors, Journal of Nuclear Medicine 49, 1132–1140 (2008). [PubMed: 18552140]

[12]. Kang HG, Ko GB, Rhee JT, Kim KM, Lee JS, and Hong SJ, A dual-ended readout detector using a meantime method for SiPM TOF-DOI PET, IEEE Transactions on Nuclear Science 62, 1935–1943 (2015).

[13]. Kuang Z. et al. , Dual-ended readout small animal PET detector by using 0.5 mm pixelated LYSO crystal arrays and SiPMs, Nuclear Instruments and Methods in Physics Research Section A: Accelerators, Spectrometers, Detectors and Associated Equipment 917, 1–8 (2019).

[14]. Van Der Laan D, Maas M, De Jong H, Schaart D, Bruyndonckx P, Lemaitre C, and Van Eijk C, Simulated performance of a small-animal PET scanner based on monolithic scintillation detectors, Nuclear Instruments and Methods in Physics Research Section A: Accelerators, Spectrometers, Detectors and Associated Equipment 571, 227–230 (2007).

[15]. Schaart DR, van Dam HT, Seifert S, Vinke R, Dendooven P, Löhner H, and Beekman FJ, A novel, SiPM-array-based, monolithic scintillator detector for PET, Physics in Medicine & Biology 54, 3501 (2009). [PubMed: 19443953]

[16]. Kaul M, Surti S, and Karp J, Combining surface treatments with shallow slots to improve the spatial resolution performance of continuous, thick LYSO detectors for PET, IEEE transactions on nuclear science 60, 44–52 (2013). [PubMed: 24077642]

[17]. Krishnamoorthy S, Blankemeyer E, Mollet P, Surti S, Van Holen R, and Karp JS, Performance evaluation of the MOLECUBES β-CUBE—a high spatial resolution and high sensitivity small animal PET scanner utilizing monolithic LYSO scintillation detectors, Physics in Medicine & Biology 63, 155013 (2018). [PubMed: 29938684]

[18]. Stockhoff M, Decuyper M, Van Holen R, and Vandenberghe S, High-resolution monolithic LYSO detector with 6-layer depth-of-interaction for clinical PET, Physics in Medicine & Biology 66, 155014 (2021).

[19]. Ito M, Lee MS, and Lee JS, Continuous depth-of-interaction measurement in a single-layer pixelated crystal array using a single-ended readout, Physics in Medicine & Biology 58, 1269 (2013). [PubMed: 23384966]

[20]. Kuang Z. et al. , Performance of a depth encoding PET detector module using light sharing and single-ended readout with SiPMs, Physics in Medicine & Biology 64, 085012 (2019). [PubMed: 30893674]

[21]. Pizzichemi M, Polesel A, Stringhini G, Gundacker S, Lecoq P, Tavernier S, Paganoni M, and Auffray E, On light sharing TOF-PET modules with depth of interaction and 157 ps FWHM coincidence time resolution, Physics in Medicine & Biology 64, 155008 (2019). [PubMed: 31239430]

[22]. Yoshida E, Obata F, Kamada K, Yoshikawa A, and Yamaya T, Development of crosshair light sharing PET detector with TOF and DOI capabilities using fast LGSO scintillator, Physics in Medicine & Biology 66, 225003 (2021).

[23]. LaBella A, Zhao W, Lubinsky R, and Goldan AH, Prismatoid light guide array for enhanced gamma ray localization in PET: a Monte Carlo simulation study of scintillation photon transport, Physics in Medicine & Biology 65, 18LT01 (2020).

[24]. LaBella A, Cao X, Petersen E, Lubinsky R, Biegon A, Zhao W, and Goldan AH, High-Resolution Depth-Encoding PET Detector Module with Prismatoid Light-Guide Array, Journal of Nuclear Medicine 61, 1528–1533 (2020). [PubMed: 32111684]

[25]. Cao X, Labella A, Zeng X, Zhao W, and Goldan AH, Depth of Interaction and Coincidence Time Resolution Characterization of Ultrahigh Resolution Time-of-Flight Prism-PET Modules, IEEE Transactions on Radiation and Plasma Medical Sciences 6, 529–536 (2021).

[26]. LaBella A, Cao X, Zeng X, Zhao W, and Goldan AH, Sub-2 mm depth of interaction localization in PET detectors with prismatoid light guide arrays and single-ended readout using convolutional neural networks, Medical Physics 48, 1019–1025 (2021). [PubMed: 33305482]

[27]. Wang Z. et al. , High-resolution and high-sensitivity PET for quantitative molecular imaging of the monoaminergic nuclei: A GATE simulation study, Medical Physics 49, 4430–4444 (2022). [PubMed: 35390182]

[28]. Zeng X. et al. , A conformal TOF-DOI Prism-PET prototype scanner For high resolution quantitative neuroimaging, Medical physics 50, 3401–3417 (2023).

[29]. Surti S, Update on time-of-flight PET imaging, Journal of Nuclear Medicine 56, 98–105 (2015). [PubMed: 25525181]

[30]. Vandenberghe S, Mikhaylova E, D'Hoe E, Mollet P, and Karp JS, Recent developments in time-of-flight PET, EJNMMI physics 3, 1–30 (2016). [PubMed: 26782039]

[31]. Conti M and Bendriem B, The new opportunities for high time resolution clinical TOF PET, Clinical and Translational Imaging 7, 139–147 (2019).

[32]. Moses WW and Derenzo S, Prospects for time-of-flight PET using LSO scintillator, IEEE Transactions on Nuclear Science 46, 474–478 (1999).

[33]. Shibuya K, Nishikido F, Tsuda T, Kobayashi T, Lam C, Yamaya T, Yoshida E, Inadama N, and Murayama H, Timing resolution improvement using DOI information in a four-layer scintillation detector for TOF-PET, Nuclear Instruments and Methods in Physics Research Section A: Accelerators, Spectrometers, Detectors and Associated Equipment 593, 572–577 (2008).

[34]. Loignon-Houle F, Toussaint M, Lee MS, Cates JW, and Lecomte R, Experimental validation of a coincidence time resolution metric including depth-of-interaction bias for TOF-PET, Physics in Medicine & Biology 65, 245004 (2020). [PubMed: 32693396]

[35]. Pizzichemi M, Stringhini G, Niknejad T, Liu Z, P Lecoq S Tavernier, J. Varela, M. Paganoni, and E. Auffray, A new method for depth of interaction determination in PET detectors, Physics in Medicine & Biology 61, 4679 (2016). [PubMed: 27245174]

[36]. Yamamoto K, Nagano T, Yamada R, Ito T, and Ohashi Y, Recent development of mppc at hamamatsu for photon counting applications, in Proceedings of the 5th international Workshop on New Photon-Detectors (PD18), page 011001, 2019.

[37]. Jan S. et al. , GATE: a simulation toolkit for PET and SPECT, Physics in Medicine & Biology 49, 4543 (2004). [PubMed: 15552416]

[38]. Di Francesco A, Bugalho R, Oliveira L, Pacher L, Rivetti A, Rolo M, Silva J, Silva R, and Varela J, TOFPET2: a high-performance ASIC for time and amplitude measurements of SiPM signals in time-of-flight applications, Journal of Instrumentation 11, C03042 (2016).

[39]. Bugalho R. et al. , Experimental characterization of the TOFPET2 ASIC, Journal of Instrumentation 14, P03029 (2019).

[40]. Nadig V, Schug D, Weissler B, and Schulz V, Evaluation of the PETsys TOFPET2 ASIC in multichannel coincidence experiments, EJNMMI physics 8, 1–21 (2021). [PubMed: 33409746]

[41]. Li Y, Zeng X, and Goldan AH, Decision Tree-Based Demultiplexing for Prism-PET, IEEE Transactions on Nuclear Science 70, 1425–1430 (2023). [PubMed: 38680514]

[42]. Krishna K and Murty MN, Genetic K-means algorithm, IEEE Transactions on Systems, Man, and Cybernetics, Part B (Cybernetics) 29, 433–439 (1999).

[43]. Association NEM, Performance Measurements of Positron Emission Tomographs (PET)., NEMA Standards Publication, NU 2-2018, 41 (2018).

[44]. Nadig V, Yusopova M, Radermacher H, Schug D, Weissler B, Schulz V, and Gundacker S, A comprehensive study on the timing limits of the TOFPET2 ASIC and on approaches for improvements, IEEE Transactions on Radiation and Plasma Medical Sciences 6, 893–903 (2022).

[45]. LaBella A, Petersen E, Cao X, Zeng X, Zhao W, and Goldan A, 36-to-1 Multiplexing with Prism-PET for High Resolution TOF-DOI PET, Journal of Nuclear Medicine 62 (supplement 1), 38 (2021).

[46]. Li Y, LaBella A, Zeng X, Wang Z, Petersen E, Cao X, Zhao W, and Goldan AH, Interleaved signal multiplexing readout in depth encoding prism-PET detectors, Medical Physics 50, 4234–4243 (2023). [PubMed: 37191309]

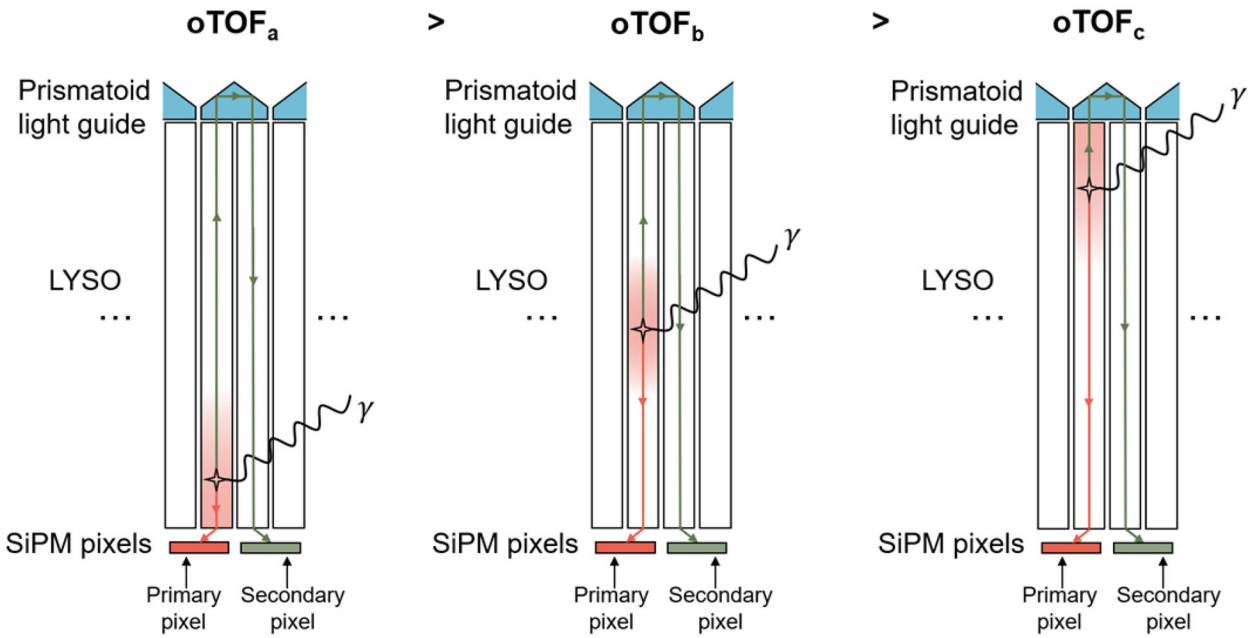

Figure 1.
Three different scenarios in which gamma photons interact with Prism-PET module at different DOI.

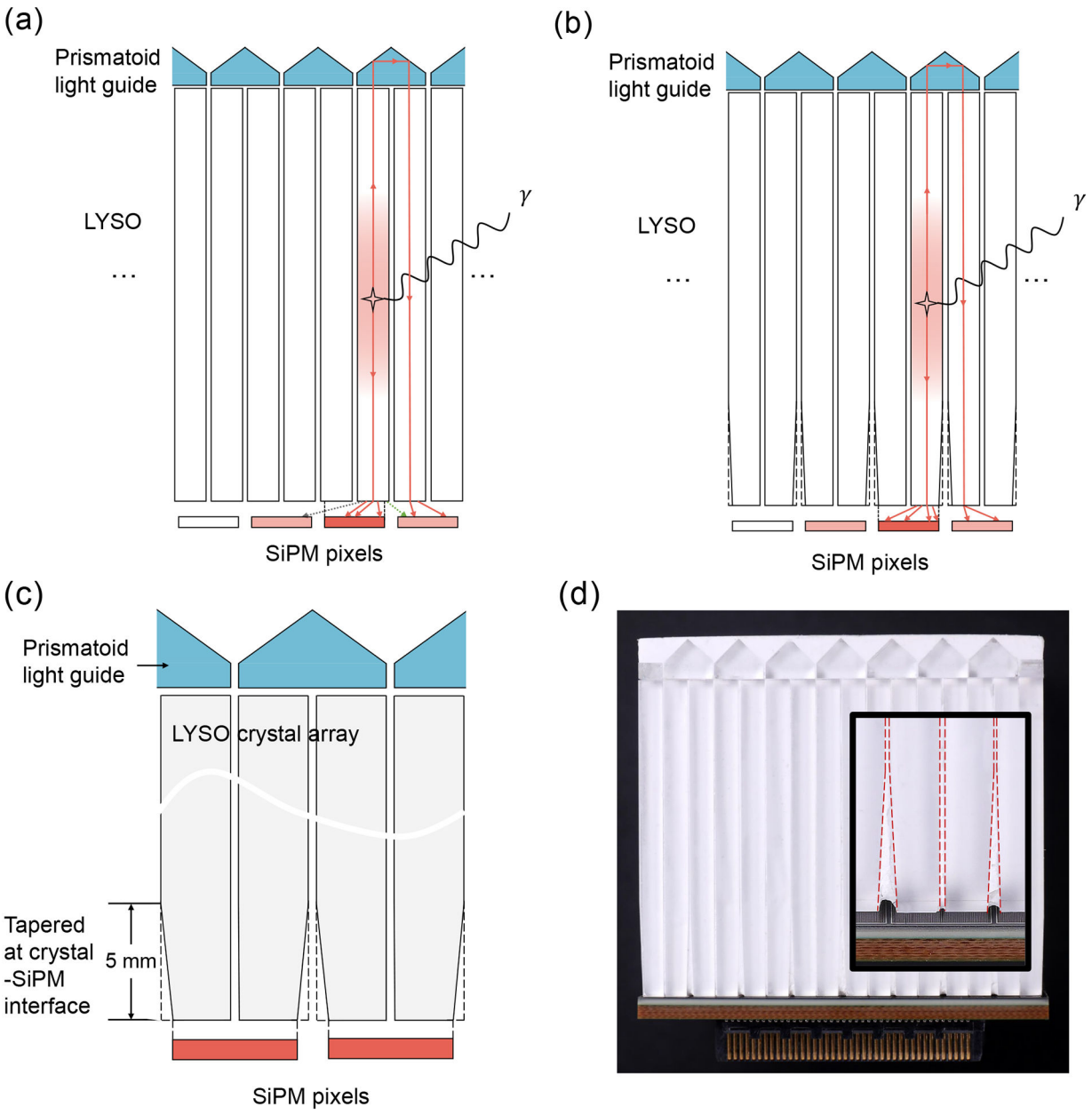

Figure 2.

(a) Light leak (dashed arrows) due to the finite gap between crystal and SiPM, which is the summation of the thickness of the coupling glue and protective resin, and due to the crystal column extending beyond the pixel's active area. (b) Light leak is minimized by the tapered design. (c) Zoom-in schematic and (d) fabricated cross-sectional views of a 4-to-1 coupled Prism-PET detector module that crystals start tapering at 5 mm from the crystal-readout interface.

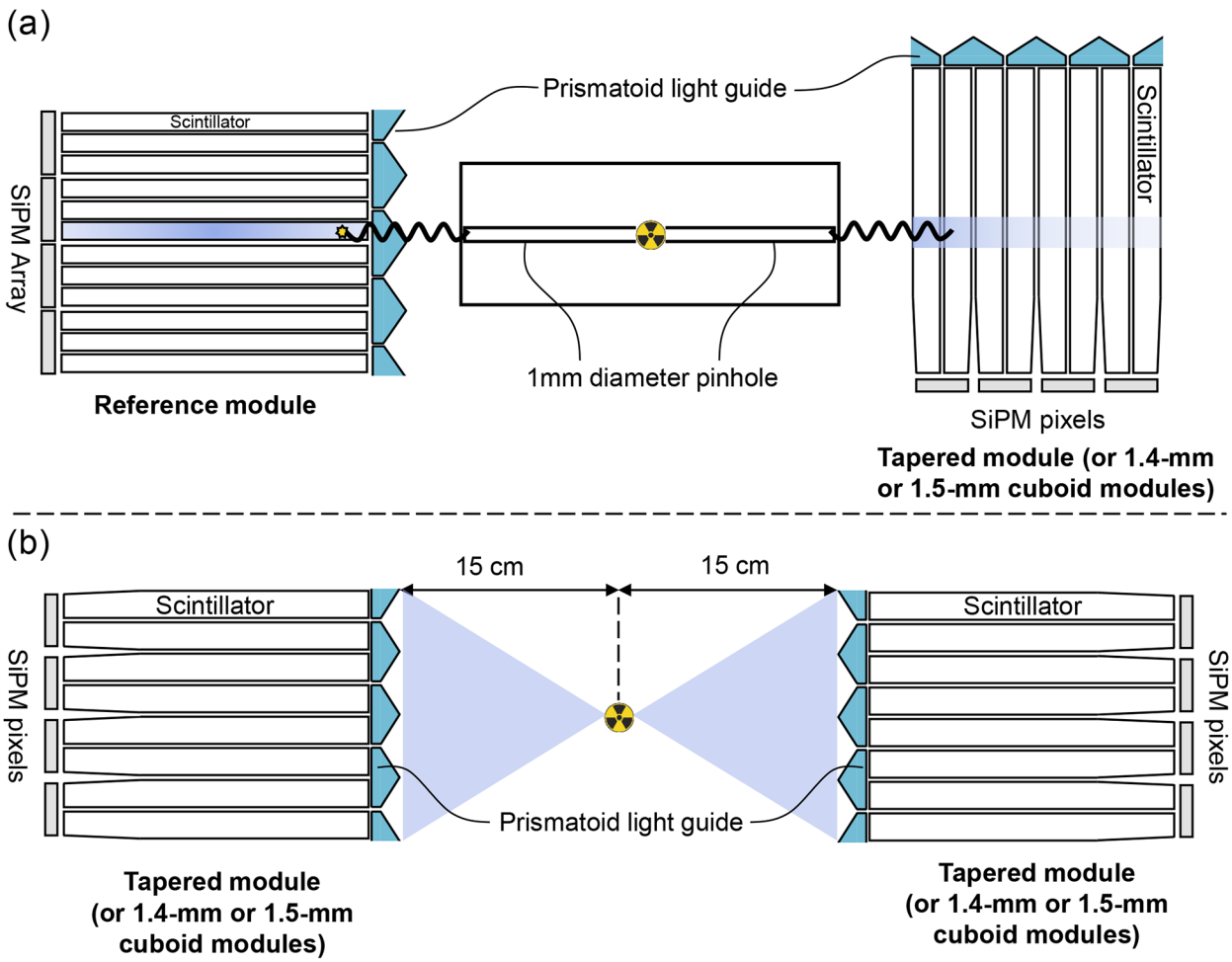

Figure 3.
Schematics of experimental setups: (a) DOI measurement, (b) Timing measurement.

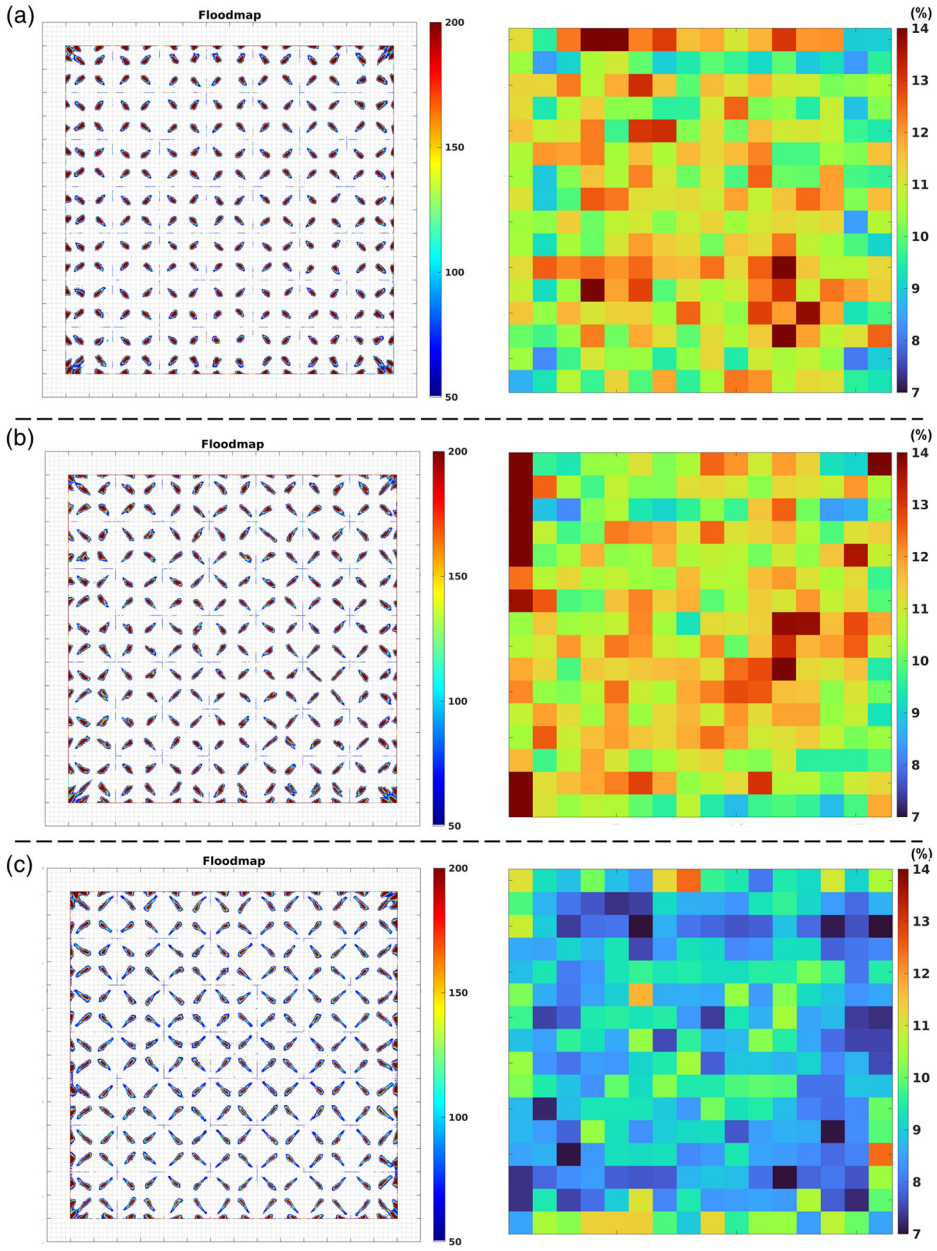

Figure 4.

Flood histograms and energy resolutions (uncorrected for saturation) for the (a) 1.4-mm cuboid, (b) 1.5-mm cuboid, and (c) 1.5-mm tapered Prism-PET module obtained with ^{22}Na uniform irradiation.

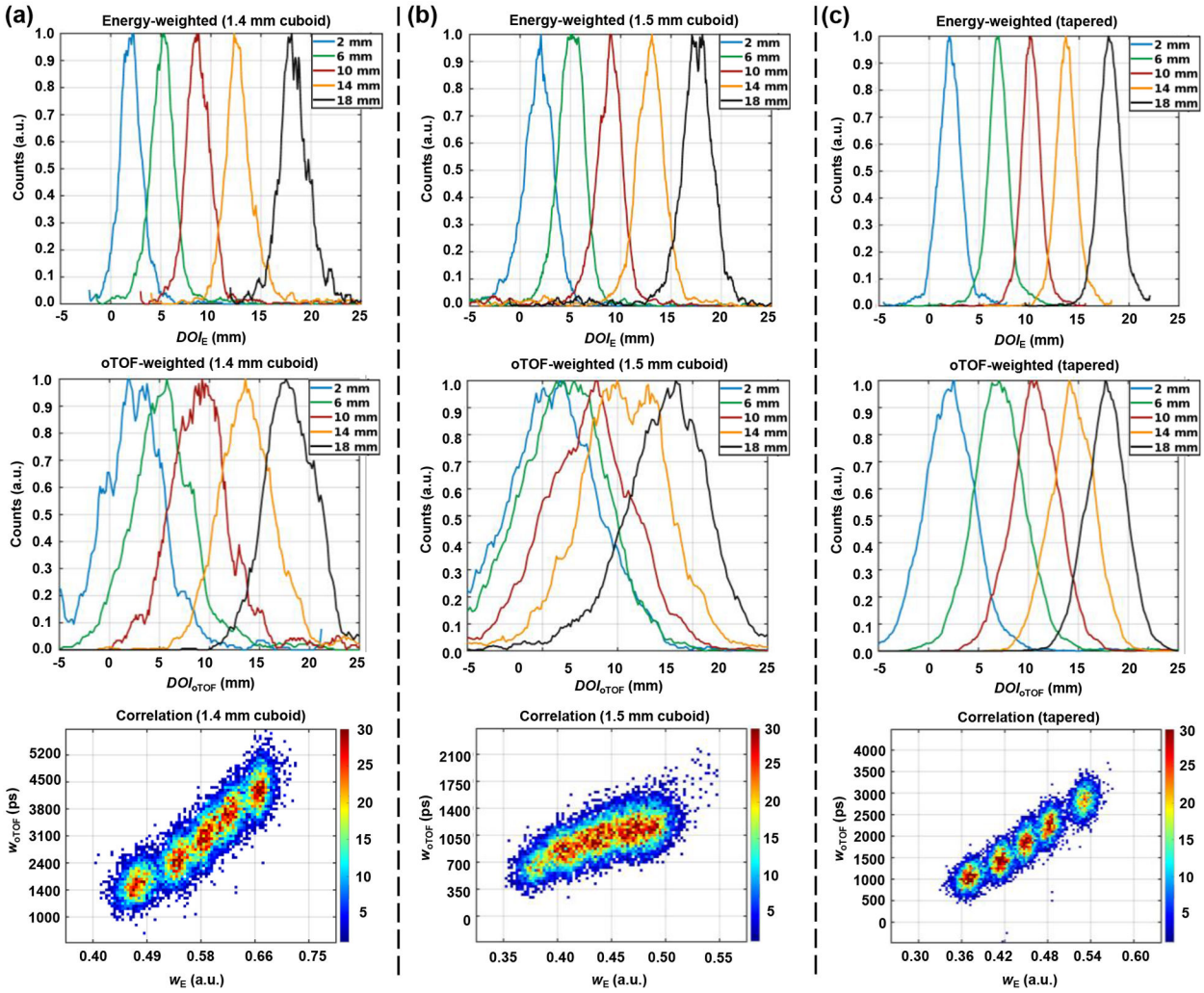

Figure 5.

Energy-weighted (w_E) DOI distributions, oTOF-weighted (w_{oTOF}) DOI distributions, and correlation between w_E and w_{oTOF} for (a) 1.4-mm cuboid, (b) 1.5-mm cuboid, and (c) tapered Prism-PET detector module at five depths (2, 6, 10, 14, and 18mm).

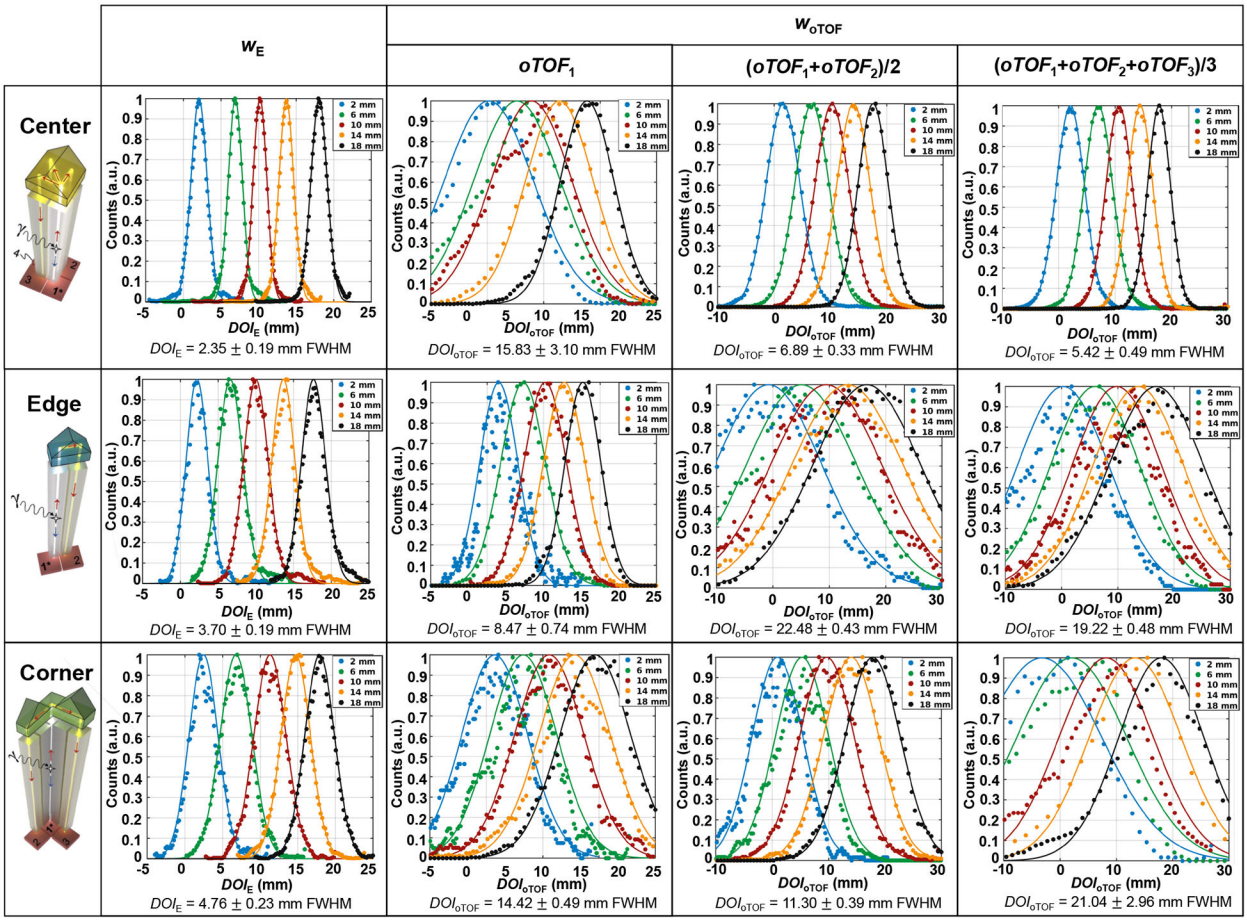

Figure 6.

DOI_E and DOI_{oTOF} distributions for center, edge, and corner crystals in the tapered Prism-PET module at five depths (2, 6, 10, 14, and 18mm).

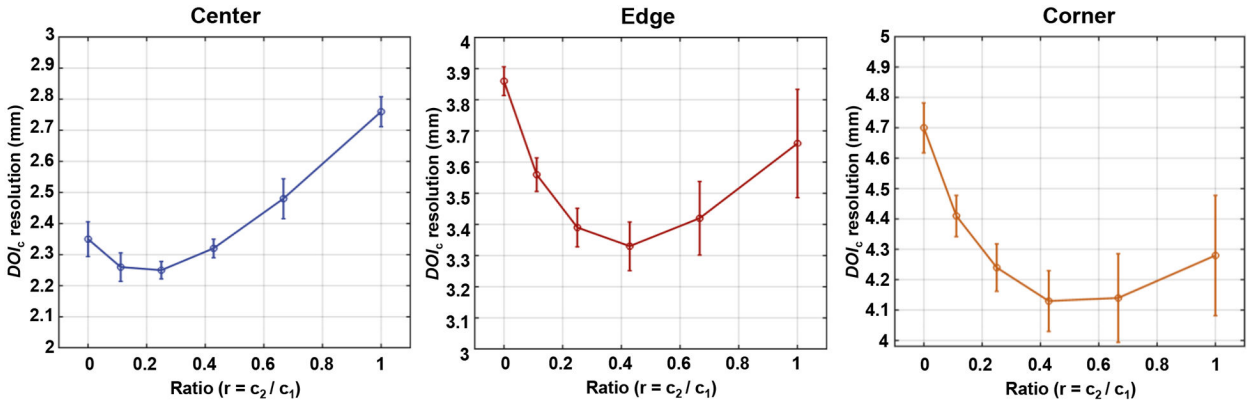

Figure 7.
DOI_c resolutions as a function of ratio r.

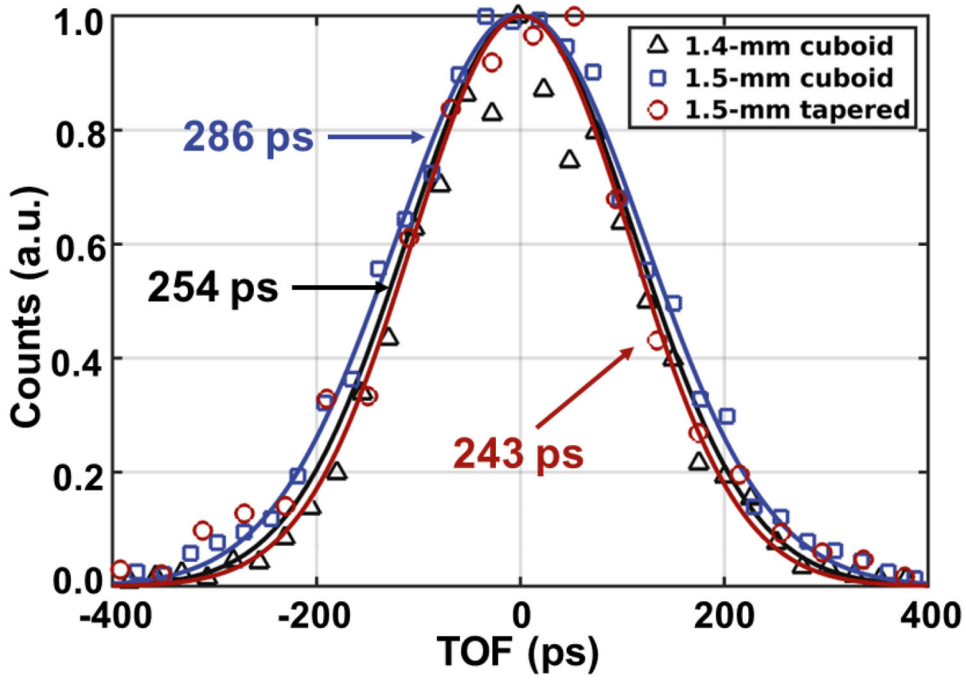

Figure 8.

Timing spectra of the 1.4-mm cuboid (black triangle), 1.5-mm cuboid (blue square), and tapered (red circle) Prism-PET module using time offset correction with 3D channels including LSTS correction and LOR-based fine-tuning.

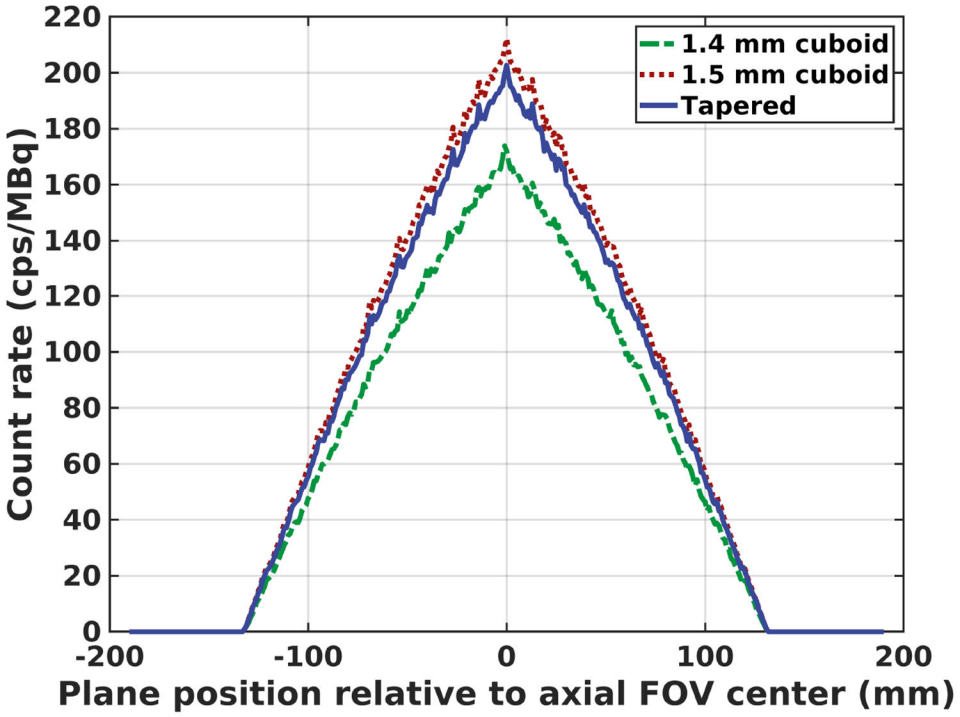

Figure 9.

Axial sensitivity profiles of 10-ring Prism-PET brain scanner with 1.4-mm cuboid (green), 1.5-mm cuboid (red), and tapered (blue) modules.